



## The directional isotropy of LIGO-Virgo binaries

4 MAXIMILIANO ISI ,<sup>1</sup> WILL M. FARR ,<sup>1,2</sup> AND VIJAY VARMA <sup>3,4,\*</sup>

5 <sup>1</sup>*Center for Computational Astrophysics, Flatiron Institute, 162 5th Ave, New York, NY 10010*

6 <sup>2</sup>*Department of Physics and Astronomy, Stony Brook University, Stony Brook NY 11794, USA*

7 <sup>3</sup>*Max Planck Institute for Gravitational Physics (Albert Einstein Institute), Am Mühlenberg 1, Potsdam 14476, Germany*

8 <sup>4</sup>*Department of Mathematics, Center for Scientific Computing and Data Science Research, University of Massachusetts, Dartmouth, MA 02747, USA*  
9

10 (Dated: November 20, 2023)

### ABSTRACT

11 We demonstrate how to constrain the degree of absolute alignment of the total angular momenta of  
12 LIGO-Virgo binary black holes, looking for a special direction in space that would break isotropy. We  
13 also allow for inhomogeneities in the distribution of black holes over the sky. Making use of dipolar  
14 models for the spatial distribution and orientation of the sources, we analyze 57 signals with false-  
15 alarm rates  $\leq 1/\text{yr}$  from the third LIGO-Virgo observing run. Accounting for selection biases, we  
16 find the population of LIGO-Virgo black holes to be consistent with both homogeneity and isotropy.  
17 We additionally find the data to constrain some directions of alignment more than others, **discuss**  
18 **the interpretation of this measurement** and produce posteriors for the directions of total angular  
19 momentum of all binaries in our set. **While our current constraints are weak, the fact that**  
20 **such a small number of detections can already yield a measurement suggests that this will**  
21 **be a powerful tool in the future; we explore this prospect with a number of simulated**  
22 **catalogs of varying size.** All code and data are made publicly available in [https://github.com/](https://github.com/maxisi/gewisotropy/)  
23 [maxisi/gewisotropy/](https://github.com/maxisi/gewisotropy/).

### 1. INTRODUCTION

25 With the increasing number of BBHs detected by  
26 LIGO (Aasi et al. 2015) and Virgo (Acernese et al.  
27 2015), it has become possible to study the distribu-  
28 tion of such gravitational wave (GW) sources over time  
29 and space (Abbott et al. 2021a; Fishbach et al. 2018,  
30 2021; Stiskalek et al. 2021; Payne et al. 2020; Cavaglia  
31 & Modi 2020; Essick et al. 2023). Since BBHs can be  
32 detected up to nonnegligible redshifts (currently,  $\lesssim 1$ ),  
33 we expect their distribution at large scales to reflect  
34 the homogeneity and isotropy that characterize the uni-  
35 verse cosmologically—a departure from that expectation  
36 would reveal a major shortcoming in our understanding

38 of the detection biases affecting the LIGO-Virgo instru-  
39 ments, or, more tantalizingly, point to fundamentally  
40 new physics or astrophysics.

41 The homogeneity (Stiskalek et al. 2021; Payne et al.  
42 2020; Cavaglia & Modi 2020; Essick et al. 2023) and  
43 isotropy (Vitale et al. 2022) of BBHs have been stud-  
44 ied before under different frameworks. In this work,  
45 we reconsider the problem from a new point of view  
46 by quantifying the degree of alignment of the BBH or-  
47 bits; in other words, we ask the question: could the to-  
48 tal angular momentum vectors of LIGO-Virgo BBHs be  
49 preferentially aligned with a special direction in space?  
50 We consider this possibility as we simultaneously search  
51 for angular inhomogeneities in the spatial distribution  
52 of sources, thus constraining the existence of special di-  
53 rections controlling both the alignment and location of  
54 BBHs.

55 Unlike previous studies, we look for a breaking of  
56 isotropy in the angular momenta through the existence  
57 of a special direction in space with reference to some

79 misi@flatironinstitute.org

80 will.farr@stonybrook.edu

81 vijay.varma@aei.mpg.de

82 \* Marie Curie fellow

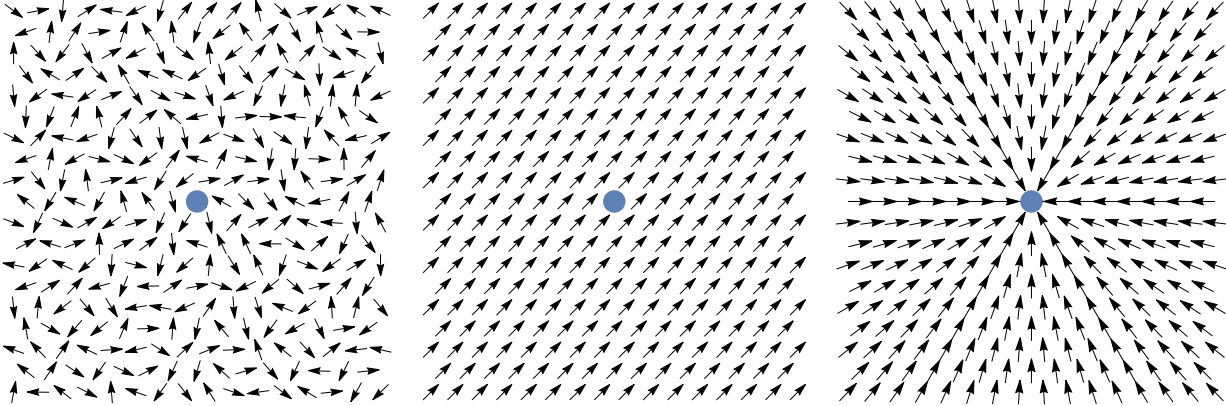


**Figure 1. BBH orientation models.** By default, we expect BBH angular momenta (arrows) to be oriented randomly with respect to Earth (circle) or each other, reflecting isotropy (first panel). In this study, we consider the possibility that BBH orbits follow a special direction in space, the extreme of which is full alignment (second panel). Previous studies, like Vitale et al. (2022), have considered models in which binaries are (or are perceived to be) aligned anomalously with respect to Earth, e.g., pointing preferentially towards it (third panel). The first two panels both have a distribution of inclinations that looks isotropic to analyses like Vitale et al. (2022).

absolute frame, like the cosmic microwave background or far away stars (Fig. 1, second panel), and not with respect to Earth. The discovery of such a special direction could reveal the presence of a vector field breaking Lorentz symmetry. This differs from **the previous work in Vitale et al. (2022)**, which checked for anomalies in the alignment of sources with respect to Earth, as reflected in the distribution of BBH inclinations relative to the line of sight (Fig. 1, third panel), **or in Okounkova et al. (2023)**, which looked for evidence of birefringence in the distribution of detected inclinations. Such studies are not sensitive to the kind of overall alignment in absolute space that we look for here.

In Sec. 2 we describe the population model we use to constrain anisotropies, as well as our assumptions about the astrophysical distribution of BBH properties like masses and redshifts, and our treatment of selection biases. In Sec. 3 we outline the data products used in our analysis. We present our results in Sec. 4, including constraints on the degree of orientation and location inisotropies, as well as maps of possible preferred directions. In Sec. 5, we summarize validation tests of our infrastructure to contextualize our measurement. We conclude in Sec. 6. Appendices show how to obtain posteriors on the angular-momentum direction, discuss hyperparameter prior choices and display posteriors for the angular-momentum direction for all events in our set.

## 2. METHOD

### 2.1. Isotropy modeling

In order to study the spatial distribution and orientation of BBHs, we must look for spatial and directional correlations in the sources we have

**detected.** This requires modeling the distribution of source locations,  $\hat{N}$ , and total-angular-momentum directions,  $\hat{J}$ . For modeling purposes, the  $\hat{N}$  and  $\hat{J}$  vectors must be expressed through their Cartesian components in some absolute reference frame.

We choose to work in geocentric, equatorial celestial coordinates, with the vernal equinox as the  $x$  axis. In that frame, the sky-location vector is, for each BBH,

$$\hat{N} = (\cos \alpha \cos \delta, \sin \alpha \cos \delta, \sin \delta), \quad (1)$$

for the right ascension  $\alpha$  and declination  $\delta$ ; meanwhile, the orientation vector is  $\hat{J} \equiv \vec{J}/|\vec{J}|$  where

$$\vec{J} = \vec{L} + \vec{S}_1 + \vec{S}_2, \quad (2)$$

for the orbital angular momentum  $\vec{L}$  and individual (dimensionful) black hole (BH) spin angular momenta  $\vec{S}_{1/2}$ . The Cartesian components of  $\hat{J}$  can be computed in the above frame as a function of  $\alpha$ ,  $\delta$ , and the polarization angle  $\psi$  (Isi 2023), as well as the component masses  $m_{1/2}$ , the dimensionless spin vectors  $\vec{\chi}_{1/2}$  and the orbital phase  $\phi_{\text{ref}}$  at some reference frequency  $f_{\text{ref}}$ ; we outline this calculation in Appendix A and release relevant code in Isi et al. (2023). We prefer to work with  $\hat{J}$  rather than  $\hat{L}$  because the former is conserved over the coalescence to a high degree, even for precessing systems (Poisson & Will 2014).

Our goal is to quantify the degree of isotropy in  $\hat{N}$  and  $\hat{J}$ . As in Essick et al. (2023), this requires analyzing the collection of detections under a hierarchical population model that allows for variable degrees of correlations: if there are no evident correlations between the sets of observed  $\hat{N}$  and  $\hat{J}$  vectors, then the data are consistent with

isotropy. As in any study of the collective properties of a set of sources, we must describe our catalog through a Bayesian hierarchical model with parameters controlling the properties of the distribution of sources from which our observations are drawn (Mandel et al. 2019). In our case, this means modeling the distribution of  $\hat{N}$  and  $\hat{J}$  vectors with parameters that control the degree of correlation structure, and then inferring those parameters from the data.

To this end, we model each of those vectors as drawn from an isotropic distribution with a dipolar correction of variable magnitude. This *ad hoc* modification may be generally seen as the first term in a harmonic expansion around isotropy, and is specifically well suited to capture the existence of a preferred direction in space. The dipolar components in the location and orientation distributions are defined by dipole vectors  $\vec{v}_{N/J}$  whose magnitudes control the degree of deviation from isotropy for  $\hat{N}$  and  $\hat{J}$  respectively.

Concretely, we implement the following population-level likelihood for each event (indexed by  $i$ )

$$p(\hat{N}_i, \hat{J}_i | \vec{v}_N, \vec{v}_J) \sim \frac{1}{16\pi^2} (1 + \vec{v}_N \cdot \hat{N}_i) (1 + \vec{v}_J \cdot \hat{J}_i), \quad (3)$$

for some special-direction vectors  $\vec{v}_{N/J}$ , with  $0 \leq |\vec{v}_{N/J}| < 1$ , to be inferred as hyperparameters from the collection of detections. The fully isotropic case is represented for  $\vec{v}_N = \vec{v}_J = 0$ . On the other hand, setting  $\vec{v}_J = 0$  alone allows for a nonhomogenous distribution of sources in the sky while assuming isotropic source orientations; this reduces to the “dipole” model in Essick et al. (2023). Modeling the likelihood as in Eq. (3), with  $|\vec{v}_{N/J}| < 1$ , ensures that the likelihood itself remains positive everywhere.

It is convenient to rephrase the constraint that  $0 \leq |\vec{v}_{N/J}| < 1$  by re-parameterizing the population in Eq. (3), through two corresponding, auxiliary vectors  $\vec{u}_{N/J}$  defined such that

$$\vec{v}_{N/J} = \frac{\vec{u}_{N/J}}{\sqrt{1 + |\vec{u}_{N/J}|^2}}. \quad (4)$$

In this way, we ensure  $0 \leq |\vec{v}_{N/J}| \leq 1$  for  $-\infty < \vec{u}_{N/J} < \infty$ ;  $\vec{u}_{N/J}$  are unconstrained. This “decompactifying” transformation is more effective for sampling purposes than enforcing a sharp constraint on the magnitudes of  $\vec{v}_{N/J}$ . For small  $|\vec{v}_{N/J}| \ll 1$ ,  $\vec{v}_{N/J} \simeq \vec{u}_{N/J}$  to second order in  $|\vec{v}_{N/J}|$ . As a prior, we choose a three-dimensional Gaussian distribution on the components of each  $\vec{u}_N$  and  $\vec{u}_J$ , with zero mean and standard deviation  $\sigma = 0.4$ . This choice of prior is designed to be fairly uninformative about  $\vec{v}_{N/J}$  (i.e., lacking a strong gradient) while

still peaking at  $\vec{v}_{N/J} = \vec{0}$ ; see Appendix B for a description of this feature.

## 2.2. Reweighting to an astrophysical population

Besides the location and orientation modeling described above, we need to ensure that our assumptions about the parameters of each individual BBH, like masses and redshift, are astrophysically sensible. To that end, we assume a redshift distribution that follows the Madau-Dickinson star formation rate (Madau & Dickinson 2014) in the comoving frame. For the masses, we assume a prior distribution inversely proportional to the heaviest component mass ( $\propto 1/m_1$ ) and uniform in the mass ratio (constant in  $q = m_2/m_1$ ), and restrict our sample to BHs with (posterior-median) masses in the range  $5 M_\odot < m_2 \leq m_1 < 150 M_\odot$ ; within that range, this choice is a simple approximation to the measurement in Abbott et al. (2021a). We assume the population of component spins are isotropically oriented with respect to the orbital angular momentum, with a uniform distribution over their dimensionless magnitude;<sup>1</sup> we control for this assumption in Sec. 5.2. A future analysis may fit the astrophysical distribution of these parameters jointly with the orientation and location of the binaries.

## 2.3. Selection biases

Since we are attempting to model the *intrinsic* distribution of all BBH sources, not merely those that were detected, we must account for the difference in LIGO-Virgo’s sensitivity to various sources. This is true for both intrinsic parameters, like BH masses and spin magnitudes, as well as the location and orientation parameters in which we are interested for this work (namely,  $\hat{N}$  and  $\hat{J}$ ). With knowledge of the instruments’ sensitivity over parameter space, we use the measured selection function to obtain a measurement of the intrinsic distribution of parameters out of the distribution of detected sources (Loredo 2004; Mandel et al. 2019). For population parameters  $\Lambda$ , the selection function defines a detection efficiency  $\xi(\Lambda)$  such that the overall hierarchical likelihood for our set of  $N_d$  detections  $\{d_i\}$  is

$$p(\{d_i\} | \Lambda) \propto \xi(\Lambda)^{-N_d} \prod_{i=1}^{N_d} \int p(d_i | \theta) p(\theta | \Lambda) d\theta, \quad (5)$$

where  $\theta$  are single-event-level parameters drawn from a population described by  $\Lambda$ ; in our case  $\Lambda = \{\vec{v}_N, \vec{v}_J\}$ .

<sup>1</sup> This implies that our modeling of  $\hat{J}$  following Eq. (3) can be reinterpreted as a nontrivial modeling of  $\vec{L}$  through Eq. (2).

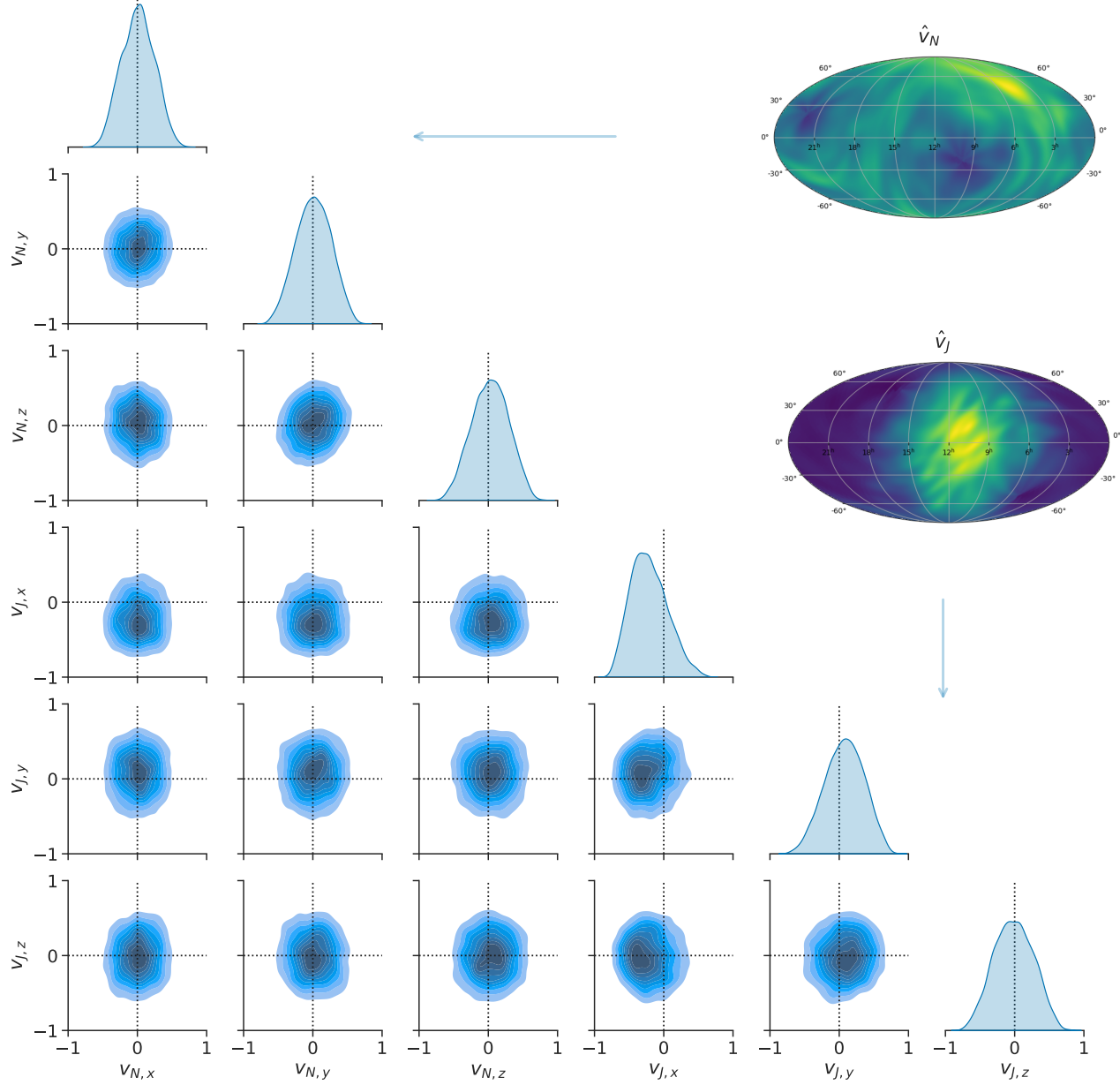


**Figure 2.** *Isotropy measurement.* Result of the simultaneous measurement of location and orientation isotropy through the model in Eq. (3), as represented by the posterior distribution on the dipole vectors  $\vec{v}_{N/J}$  (corner plot), and the corresponding projections over the sky (Mollweide insets). The six-dimensional posterior distribution is represented through credible levels over two-dimensional slices (blue contours, spaced at intervals corresponding to 10% increments in probability mass, with the outer contour enclosing 90% of the probability), and one-dimensional marginals (diagonal). The upper-left and lower-right sub-corners encode constraints on the individual components of each  $\vec{v}_N$  and  $\vec{v}_J$  respectively (highlighted with vertical and horizontal lines in the margin), while the other panels encode potential correlations between the location and orientation inisotropies. The measurements for  $\vec{v}_{N/J}$  can be projected into distribution over the sky as in the top-right insets, which show the allowed dipole orientations for  $\hat{v}_N \equiv \vec{v}_N / |\vec{v}_N|$  (top) or  $\hat{v}_J \equiv \vec{v}_J / |\vec{v}_J|$  (bottom), with lighter colors encoding higher probability density over the celestial sphere (Singer 2018; Singer et al. 2016a,b); inhomogeneities in these sky-maps do not constitute evidence for anisotropies. Isotropy is recovered for  $\vec{v}_N = \vec{v}_J = 0$  (dotted lines), which is well supported by the 6D posterior.



**Table 1.** Events considered.

GW190408_181802	GW190708_232457	GW191129_134029
GW190412_053044	GW190719_215514	GW191204_171526
GW190413_052954	GW190720_000836	GW191215_223052
GW190413_134308	GW190727_060333	GW191216_213338
GW190421_213856	GW190728_064510	GW191222_033537
GW190503_185404	GW190731_140936	GW191230_180458
GW190512_180714	GW190803_022701	GW200112_155838
GW190513_205428	GW190805_211137	GW200128_022011
GW190517_055101	GW190828_063405	GW200129_065458
GW190519_153544	GW190828_065509	GW200202_154313
GW190521_030229	GW190910_112807	GW200208_130117
GW190521_074359	GW190915_235702	GW200209_085452
GW190527_092055	GW190925_232845	GW200216_220804
GW190602_175927	GW190929_012149	GW200219_094415
GW190620_030421	GW190930_133541	GW200224_222234
GW190630_185205	GW191103_012549	GW200225_060421
GW190701_203306	GW191105_143521	GW200302_015811
GW190706_222641	GW191109_010717	GW200311_115853
GW190707_093326	GW191127_050227	GW200316_215756

Evaluating the detectors' sensitivity over parameter space,  $\xi(\Lambda)$ , requires large simulation campaigns that quantify the end-to-end performance of LIGO-Virgo detection pipelines by injecting and recovering synthetic signals. As in Essick et al. (2023), we take advantage of the BBH dataset in Abbott et al. (2021b) for this purpose.<sup>2</sup> This dataset records source parameters corresponding to  $N_{\text{rec}}$  synthetic signals recovered by LIGO-Virgo search pipelines, out of an original set of  $N_{\text{draw}}$  simulated astrophysical signals following a fiducial population  $p_{\text{draw}}(\theta)$ ; by comparing the distribution of detected versus originally drawn parameters, we can estimate  $\xi(\Lambda)$  through a Monte-Carlo integral as (Farr 2019; Essick & Farr 2022)

$$\xi(\Lambda) \simeq \frac{1}{N_{\text{draw}}} \sum_{j=1}^{N_{\text{rec}}} \frac{p(\theta_j | \Lambda)}{p_{\text{draw}}(\theta_j)}. \quad (6)$$

Since this injection campaign only covered LIGO-Virgo's third observing run, we only consider events detected during that period; together with the mass constraints cited above, this means there are 57 BBH events to be included in our analysis (listed in Table 1).

### 3. DATA

Our analysis starts from posterior samples for individual events reported by LIGO-Virgo in Abbott et al. (2021c,d) and publicly released in Abbott et al. (2022, 2021e) through the Gravitational Wave Open Science

<sup>2</sup> Specifically, the `endo3_bbhpop-LIGO-T2100113-v12` injection set.

Center (Abbott et al. 2021f,g,h). Specifically, we make use of results obtained with the IMRPhenomXPHM waveform (Pratten et al. 2021, 2020; García-Quirós et al. 2020, 2021) that have been already reweighted to a distance prior uniform in comoving volume. The single-event inference was carried out by the LIGO-Virgo collaborations using the BILBY parameter estimation pipeline (Romero-Shaw et al. 2020; Ashton et al. 2019), as detailed in Abbott et al. (2021c,d). We reweight those samples so that they follow an effective prior corresponding to the astrophysical population described in Sec. 2.2; this entails taking draws from the set of posterior samples with a weight proportional to the ratio of the desired astrophysical prior to the fiducial prior used by LIGO-Virgo during sampling (see, e.g., Miller et al. 2020, for details). We then use these samples to produce distributions for the components of  $\hat{N}$  and  $\hat{J}$ , which we take as input for our hierarchical analysis based on Eq. (3).

The six-dimensional posteriors for the components of  $\hat{J}$  and  $\hat{N}$  for each event are the primary input for our hierarchical isotropy analysis. We show the posteriors for  $\hat{J}$  in Fig. 8 as skymaps for all events in our set, produced using standard LIGO-Virgo tools for representing probability densities over the sky (Singer 2018; Singer et al. 2016a,b); we make these posteriors, resulting from the calculation detailed in Appendix A, available in our data release (Isi et al. 2023). The equivalent figures for  $\hat{N}$  are nothing but the sky-localization maps already made available by LIGO-Virgo (Abbott et al. 2022, 2021e).

### 4. RESULTS

We showcase the full result of our analysis in Fig. 2, which represents the simultaneous measurement of location and orientation anisotropies through the six-dimensional posterior on the components of  $\vec{v}_N$  and  $\vec{v}_J$ . The result is fully consistent with both kinds of isotropy, with  $\vec{v}_N = 0$  and  $\vec{v}_J = 0$  supported with high credibility, falling close to the peak of the marginal distributions on the 1% and 49% quantiles respectively;<sup>3</sup> this feature is also reflected in the fact that the origin is well supported in all the panels of the corner plot in Fig. 2. The result for  $\vec{v}_N$  is consistent with previous studies (Essick et al. 2023), which did not find evidence against isotropy in the location of LIGO-Virgo sources.

To the extent that there is any support for nonzero dipolar contributions to the location or orientation densities (namely, for  $|\vec{v}_{J/N}| > 0$ ), their possible directions in the sky are represented by the insets on the top right

<sup>3</sup> These three-dimensional quantiles correspond to the fraction of  $\vec{v}_{J/N}$  samples with higher probability density than the origin.

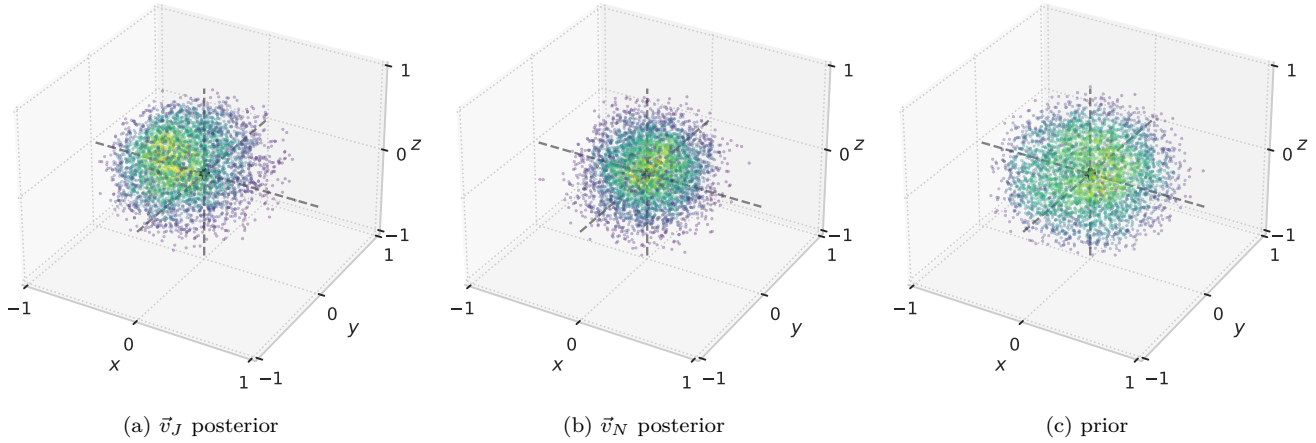


**Figure 3.** 3D distributions. Three-dimensional representation of the  $\vec{v}_{J/N}$  measurement in Fig. 2 (first two panels), in comparison to the prior (last panel). Each point is drawn from the corresponding three-dimensional distribution, with color proportional to the probability density (lighter colors for higher density). The origin, representing isotropy, is well supported in all cases (intersection of gray dashed lines). As reflected in the predominance of dark colors (low density) towards the edges, both posteriors are more tightly concentrated than the prior, indicating that the data are informative; additionally, the  $\vec{v}_J$  distribution is slightly shifted towards the negative- $x$  direction.

289 of Fig. 2: a higher density indicates a potentially allowed  
 290 orientation for the  $\vec{v}_N$  (top) or  $\vec{v}_J$  (bottom) dipole vec-  
 291 tors. These skymaps reveal that the data are not in  
 292 conflict with the existence of a weak dipole along the  
 293 vernal equinox in the celestial equatorial plane (the di-  
 294 rection of the  $x$  axis in our Cartesian coordinate system),  
 295 as implied by the marginal on  $\vec{v}_{J,x}$  in Fig. 2; this dipole  
 296 is allowed, but not required, by the data, since the pos-  
 297 terior is fully consistent with  $\vec{v}_J = 0$ .

298 Indeed, although inhomogeneities appear in these  
 299 Mollweide projections, this should not be interpreted  
 300 as evidence for anisotropies: the density of points in  
 301 those maps only encodes *permissible* directions for the  
 302 dipole, without implications for its magnitude. In fact,  
 303 inhomogeneities will appear in such plots any time the  
 304 posterior does not happen to peak exactly at the three-  
 305 dimensional origin of  $\vec{v}_{J/N}$ , as we expect to be commonly  
 306 the case even if  $\vec{v}_{J/N} = \vec{0}$  is the underlying truth.<sup>4</sup>

307 In Fig. 3, we provide an additional representation  
 308 of this posterior projected onto the three-dimensional  
 309 spaces of  $\vec{v}_J$  and  $\vec{v}_N$ ; we also present the prior for com-  
 310 parison. Large dipolar contributions are disfavored by  
 311 the posterior in all cases, and the posterior distributions  
 312 are more concentrated than the prior, indicating that  
 313 the data are informative. The posterior standard devi-

<sup>4</sup> With a finite number of events in the catalog, even if  $\vec{v}_{J/N}$  is zero in truth, the maximum-likelihood estimate will not, in general, be zero. The posterior will therefore peak away from zero (but be fully consistent with zero). In this situation inhomogeneity can appear as in Fig. 2.

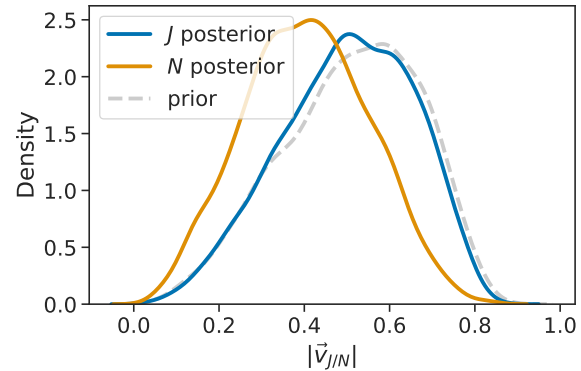


**Figure 4.** Posterior on dipole magnitudes. The measurement of Fig. 2 translated into one-dimensional posteriors on the  $|\vec{v}_J|$  (blue) and  $|\vec{v}_N|$  (orange) magnitudes. These are shifted rightward with respect to the implied prior (gray), which itself heavily disfavors  $|\vec{v}_{J/N}| = 0$  due to the reduced phase space near the origin in a three-dimensional space.

314 ations for the three Cartesian components of  $\vec{v}_J$  and  $\vec{v}_N$   
 315 are smaller by  $\{15\%, 10\%, 9\%\}$  and  $\{25\%, 20\%, 15\%\}$  re-  
 316 spectively with respect to the prior. The stronger tight-  
 317 ening in the  $\vec{v}_N$  distribution is a consequence of  $\hat{N}$  being  
 318 better constrained than  $\hat{J}$  in individual events. Figure  
 319 3 again makes it apparent that data disfavor certain di-  
 320 rections for the  $\vec{v}_J$  dipole (towards the positive- $x$  quad-  
 321 rants, away from the vernal equinox).

322 We may translate the result in Fig. 2 into a posterior  
 323 on the magnitudes  $|\vec{v}_{J/N}|$  of the dipole components, as  
 324 we do in Fig. 4. However, the one-dimensional posteriors  
 325 on these quantities is heavily dominated by the dimen-  
 326 sionality of the problem, which results in a Jacobian dis-

327 favoring small values of  $|\vec{v}_{J/N}|$  due to the limited phase  
 328 space near  $\vec{v}_J = 0$  or  $\vec{v}_N = 0$ .<sup>5</sup> Therefore, even though  
 329 our three-dimensional prior does not treat  $\vec{v}_{J/N} = 0$  as a  
 330 special point (Appendix B), the effective prior induced  
 331 on the magnitudes heavily disfavors the origin in  $|\vec{v}_{J/N}|$   
 332 due to the reduced available prior volume (gray curve in  
 333 Fig. 4); that explains why the posteriors in Fig. 4 them-  
 334 selves appear to disfavor  $|\vec{v}_{J/N}| = 0$ . With that in mind,  
 335 the influence of the data can be seen in the leftward shift  
 336 of the  $|\vec{v}_{J/N}|$  distributions with respect to the prior; this  
 337 is effect is more pronounced for  $\vec{v}_N$ , which is a conse-  
 338 quence of the fact that  $\hat{N}$  is generally better measured  
 339 than  $\hat{J}$ . Although the shift in  $|\vec{v}_J|$  is slight, the data are  
 340 informative about  $\vec{v}_J$ —constraining some of its possible  
 341 orientations (Figs. 2 and 3), if not its overall magnitude.

## 342 5. VALIDATION

343 In this section, we validate our setup by studying sim-  
 344 ulated datasets in which  $\hat{J}$  and  $\hat{N}$  are isotropically dis-  
 345 tributed (5.1). We also revisit our assumptions about  
 346 the astrophysical distribution of BBH parameters, de-  
 347 scribed in Sec. 2.2, and show that they are robust.

### 348 5.1. *Injections from selection set*

349 We validate our infrastructure on the set of injections  
 350 used to evaluate the selection function of the instru-  
 351 ments, which was drawn from an intrinsically isotropic  
 352 distribution (Abbott et al. 2021b). This provides an  
 353 end-to-end test of our setup, including the computation  
 354 of location and orientation vectors, the selection func-  
 355 tion and the inference process.

356 Concretely, we simulate catalogs of detections drawn  
 357 from the injection set used to evaluate the selection func-  
 358 tion as described in Sec. 2.3 (Abbott et al. 2021b). For  
 359 simplicity, we treat the injection parameters as a single  
 360 sample of a fictitious posterior: the input to our hierar-  
 361 chical analysis is one sample per synthetic event, drawn  
 362 from the distribution in Sec. 2.3. At each iteration, we  
 363 double the size of the simulated catalog. Since the in-  
 364 jection distribution was constructed to be isotropic (Ab-  
 365 bott et al. 2021b), we expect this experiment to indicate  
 366  $\vec{v}_{J/N} = \vec{0}$ , with certainty growing with catalog size.

367 We show the result in Fig. 5 for  $\vec{v}_J$  (the result for  
 368  $\vec{v}_N$  is similar). As expected,  $\vec{v}_{J/N} = \vec{0}$  is supported  
 369 with increasing certainty as the synthetic catalog grows.

<sup>5</sup> In other words, although the probability density is high near the origin, this is outweighed by the greater volume found far away, so that the overall probability of finding  $\vec{v}_{J/N} = 0$  is small. Any density in  $\vec{v}_{J/N}$  that is finite at the origin will produce a density on  $|\vec{v}_{J/N}|$  that behaves as  $|\vec{v}_{J/N}|^2$  near the origin.

370 This is what we expect if our infrastructure is working  
 371 as designed.

## 372 5.2. *Astrophysical distributions*

373 As described, in Sec. 2.2, analysis above (Figs. 2–4)  
 374 hinged on simplified assumptions about the astrophys-  
 375 ical distribution of BH masses, spins and redshifts. To  
 376 evaluate the impact of this simplification, we repeat our  
 377 analysis but now reweighting to a different astrophys-  
 378 ical population based on the measurements in Abbott  
 379 et al. (2021a). Specifically, we make use of the highest-  
 380 probability instantiation of the POWER LAW + PEAK  
 381 parametric mass model and the DEFAULT spin model,  
 382 with parameters obtained from the posterior samples  
 383 released in Abbott et al. (2023). This model treats the  
 384 astrophysical distribution of BH masses as a power law  
 385 plus a Gaussian peak, with density evolving over co-  
 386 moving volume as a power law; the spins are isotropic  
 387 with a possible Gaussian overdensity in alignment with  
 388 the orbital angular momentum, and with magnitudes  
 389 following a Beta distribution (see (Abbott et al. 2021a)  
 390 for details). To implement this new astrophysical prior,  
 391 both individual detections and the selection injections  
 392 are reweighted accordingly.

393 The result of assuming this different astrophysical dis-  
 394 tribution is shown in Fig. 6, compared to the main result  
 395 above. Although the new posterior differs slightly from  
 396 our primary one in Fig. 2, as we might expect given  
 397 the difference in models, the change is quite limited and  
 398 does not qualitatively impact the discussion above. The  
 399 discrepancy is somewhat more pronounced for the com-  
 400 ponents of  $\vec{v}_J$ , as we might expect from the fact that  
 401 the reconstruction of  $\hat{J}$  must factor our inference on the  
 402 masses and three dimensional spins of each BBH. In the  
 403 future, a more comprehensive analysis might simultane-  
 404 ously measure  $\vec{v}_{J/N}$  and the distribution of astrophysical  
 405 properties.

## 406 6. CONCLUSION

407 We have demonstrated a measurement constraining  
 408 the potential alignment of the total angular momenta  
 409 of BBHs detected by LIGO and Virgo, using 57 detec-  
 410 tions from their third observing run and duly account-  
 411 ing for selection effects. In addition to alignment of  
 412 momenta, we simultaneously looked for inhomogeneities  
 413 in the distribution of sources over the sky. **Although**  
 414 **the measurement is only weakly informative**, we  
 415 found no evidence against isotropy in either the orienta-  
 416 tion or, consistent with previous works, the location of  
 417 LIGO-Virgo BBHs. Additionally, we determined that  
 418 the GWTC-3 data disfavor certain orientations of the  
 419 potential preferred alignment of angular momenta more  
 420 than others.

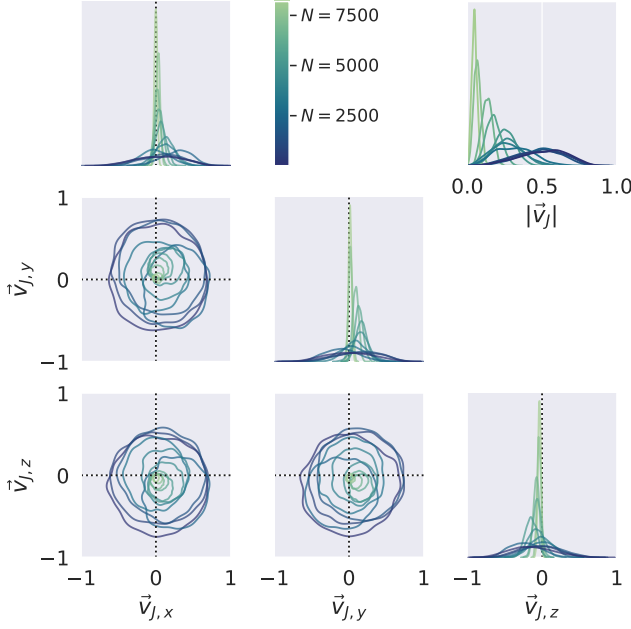


**Figure 5.** Validation on synthetic catalogs drawn from selection injection set. Result of hierarchical analyses on synthetic catalogs of increasing size  $N$  (color), obtained by taking draws from the injection set used to evaluate the selection function (Sec. 2.3) and using them as single samples from the  $\hat{J}$  and  $\hat{N}$  posterior of synthetic events. We show the posterior on the components of  $\vec{v}_J$  (main corner), and the implied posterior on the magnitude  $|\vec{v}_J|$  (upper right). A lighter color corresponds to a larger catalog: starting with  $N = 4$  events for the darkest color and progressively doubling the catalog size 11 times to reach  $N = 8192$  events for the lightest color. The hierarchical analysis measures  $\vec{v}_J = \vec{0}$  with growing precision as the size of the catalog increases.

421 Future measurements will improve as the LIGO, Virgo  
 422 and KAGRA detectors grow in sensitivity, resulting in  
 423 many more detections at higher signal-to-noise ratios,  
 424 which will result in more precise isotropy constraints.  
 425 The advent of next generation detectors, like Cosmic  
 426 Explorer (Dwyer et al. 2015; Abbott et al. 2017; Re-  
 427 itze et al. 2019) or the Einstein Telescope (Punturo  
 428 et al. 2010), will enable the exploration of higher order  
 429 anisotropies and other interesting effects, like correla-  
 430 tions with redshift or, potentially, local correlations in  
 431 the directions  $\hat{N}$  and  $\hat{J}$  on the sky.

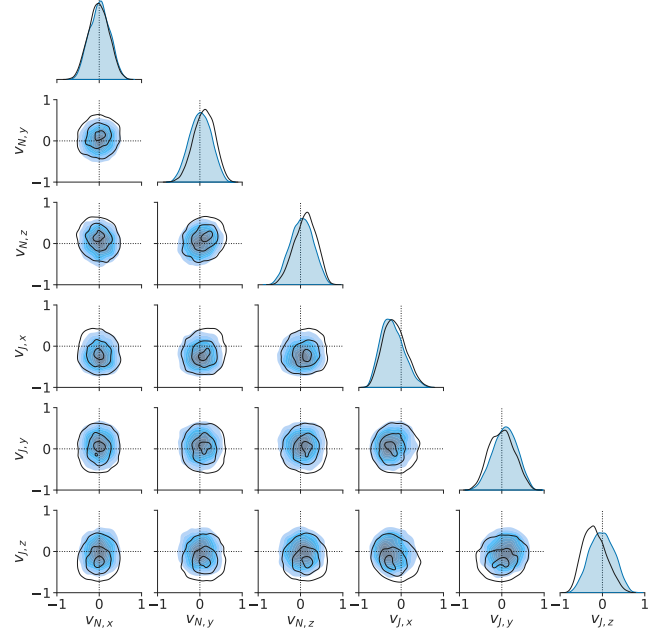


**Figure 6.** Effect of astrophysical population. We repeat the isotropy analysis with a different assumption about the underlying distribution of BBH parameters based on the measurement in Abbott et al. (2021a). This yields the result shown in black, as opposed to the result in Fig. 2, which is reproduced here in blue for comparison. The black contours enclose 90%, 50% and 10% of the marginal probability mass.



We thank Reed Essick for valuable comments. The Flatiron Institute is a division of the Simons Foundation. V.V. acknowledges funding from the European Union’s Horizon 2020 research and innovation program under the Marie Skłodowska-Curie grant agreement No. 896869. This material is based upon work supported by NSF’s LIGO Laboratory which is a major facility fully funded by the National Science Foundation. This research has made use of data or software obtained from the Gravitational Wave Open Science Center ([gw-openscience.org](http://gw-openscience.org)), a service of LIGO Laboratory, the LIGO Scientific Collaboration, the Virgo Collaboration, and KAGRA. LIGO Laboratory and Advanced LIGO are funded by the United States National Science Foundation (NSF) as well as the Science and Technology Facilities Council (STFC) of the United Kingdom, the Max-Planck-Society (MPS), and the State of Niedersachsen/Germany for support of the construction of Advanced LIGO and construction and operation of the GEO600 detector. Additional support for Advanced LIGO was provided by the Australian Research Council. Virgo is funded, through the European Gravitational Observatory (EGO), by the French Centre National de Recherche Scientifique (CNRS), the Italian Istituto Nazionale di Fisica Nucleare (INFN) and the Dutch Nikhef, with contributions by institutions from Belgium, Germany, Greece, Hungary, Ireland, Japan, Monaco, Poland, Portugal, Spain. The construction and operation of KAGRA are funded by Ministry of Education, Culture, Sports, Science and Technology (MEXT), and Japan Society for the Promotion of Science (JSPS), National Research Foundation (NRF) and Ministry of Science and ICT (MSIT) in Korea, Academia Sinica (AS) and the Ministry of Science and Technology (MoST) in Taiwan. This is a reproducible article compiled with SHOWYOURWORK ([Luger et al. 2021](#)). This paper carries LIGO document number LIGO-P2300088.

## REFERENCES

- Aasi, J., et al. 2015, Classical Quantum Gravity, 32, 074001, doi: [10.1088/0264-9381/32/7/074001](https://doi.org/10.1088/0264-9381/32/7/074001)
- Abbott, B. P., et al. 2017, Class. Quant. Grav., 34, 044001, doi: [10.1088/1361-6382/aa51f4](https://doi.org/10.1088/1361-6382/aa51f4)
- Abbott, R., et al. 2021a. <https://arxiv.org/abs/2111.03634>
- . 2021b, GWTC-3: Compact Binary Coalescences Observed by LIGO and Virgo During the Second Part of the Third Observing Run — O3 search sensitivity estimates, Zenodo, doi: [10.5281/zenodo.5546676](https://doi.org/10.5281/zenodo.5546676)
- . 2021c. <https://arxiv.org/abs/2111.03606>
- . 2021d. <https://arxiv.org/abs/2108.01045>
- . 2021e, GWTC-3: Compact Binary Coalescences Observed by LIGO and Virgo During the Second Part of the Third Observing Run — Parameter estimation data release, Zenodo, doi: [10.5281/zenodo.5546663](https://doi.org/10.5281/zenodo.5546663)
- . 2021f, GWTC-2.1 Data Release. <https://www.gw-openscience.org/GWTC-2.1/>
- . 2021g, GWTC-3 Data Release. <https://www.gw-openscience.org/GWTC-3/>
- . 2021h, SoftwareX, 13, 100658, doi: [10.1016/j.softx.2021.100658](https://doi.org/10.1016/j.softx.2021.100658)

- 495 —. 2022, GWTC-2.1: Deep Extended Catalog of Compact  
 496 Binary Coalescences Observed by LIGO and Virgo  
 497 During the First Half of the Third Observing Run -  
 498 Parameter Estimation Data Release, v2, Zenodo,  
 499 doi: [10.5281/zenodo.6513631](https://doi.org/10.5281/zenodo.6513631)
- 500 —. 2023, The population of merging compact binaries  
 501 inferred using gravitational waves through GWTC-3 -  
 502 Data release, v2, Zenodo, doi: [10.5281/zenodo.7843926](https://doi.org/10.5281/zenodo.7843926)
- 503 Acernese, F., et al. 2015, Classical Quantum Gravity, 32,  
 504 024001, doi: [10.1088/0264-9381/32/2/024001](https://doi.org/10.1088/0264-9381/32/2/024001)
- 505 Anderson, W. G., Brady, P. R., Chin, D., et al. 2002, Beam  
 506 pattern response functions and times of arrival for  
 507 earthbound interferometer, Tech. Rep. LIGO-T010110,  
 508 LIGO Scientific Collaboration.  
<https://dcc.ligo.org/LIGO-T010110/public>
- 510 Ashton, G., et al. 2019, Astrophys. J. Suppl., 241, 27,  
 511 doi: [10.3847/1538-4365/ab06fc](https://doi.org/10.3847/1538-4365/ab06fc)
- 512 Bohe, A., Marsat, S., Faye, G., & Blanchet, L. 2013, Class.  
 513 Quant. Grav., 30, 075017,  
 514 doi: [10.1088/0264-9381/30/7/075017](https://doi.org/10.1088/0264-9381/30/7/075017)
- 515 Cavaglia, M., & Modi, A. 2020, Universe, 6, 93,  
 516 doi: [10.3390/universe6070093](https://doi.org/10.3390/universe6070093)
- 517 Creighton, J., Fairhurst, S., Krishnan, B., et al. 2008,  
 518 LALSimulation-LALInference parameter transformations.  
[https://lscsoft.docs.ligo.org/lalsuite/lalsimulation/group\\_\\_lalsimulation\\_\\_inference.html#ga1517b28ff879d5d1c7ba8468385e4054](https://lscsoft.docs.ligo.org/lalsuite/lalsimulation/group__lalsimulation__inference.html#ga1517b28ff879d5d1c7ba8468385e4054)
- 522 Dwyer, S., Sigg, D., Ballmer, S. W., et al. 2015, Phys. Rev.,  
 523 D91, 082001, doi: [10.1103/PhysRevD.91.082001](https://doi.org/10.1103/PhysRevD.91.082001)
- 524 Essick, R., & Farr, W. 2022.  
<https://arxiv.org/abs/2204.00461>
- 526 Essick, R., Farr, W. M., Fishbach, M., Holz, D. E., &  
 527 Katsavounidis, E. 2023, Phys. Rev. D, 107, 043016,  
 528 doi: [10.1103/PhysRevD.107.043016](https://doi.org/10.1103/PhysRevD.107.043016)
- 529 Farr, W. M. 2019, Research Notes of the AAS, 3, 66,  
 530 doi: [10.3847/2515-5172/ab1d5f](https://doi.org/10.3847/2515-5172/ab1d5f)
- 531 Fishbach, M., Holz, D. E., & Farr, W. M. 2018, Astrophys.  
 532 J. Lett., 863, L41, doi: [10.3847/2041-8213/aad800](https://doi.org/10.3847/2041-8213/aad800)
- 533 Fishbach, M., Doctor, Z., Callister, T., et al. 2021,  
 534 Astrophys. J., 912, 98, doi: [10.3847/1538-4357/abee11](https://doi.org/10.3847/1538-4357/abee11)
- 535 García-Quirós, C., Colleoni, M., Husa, S., et al. 2020, Phys.  
 536 Rev. D, 102, 064002, doi: [10.1103/PhysRevD.102.064002](https://doi.org/10.1103/PhysRevD.102.064002)
- 537 García-Quirós, C., Husa, S., Mateu-Lucena, M., &  
 538 Borchers, A. 2021, Class. Quant. Grav., 38, 015006,  
 539 doi: [10.1088/1361-6382/abc36e](https://doi.org/10.1088/1361-6382/abc36e)
- 540 Harris, C. R., et al. 2020, Nature, 585, 357,  
 541 doi: [10.1038/s41586-020-2649-2](https://doi.org/10.1038/s41586-020-2649-2)
- 542 Hunter, J. D. 2007, Computing In Science & Engineering,  
 543 9, 90, doi: [10.1109/MCSE.2007.55](https://doi.org/10.1109/MCSE.2007.55)
- 544 Isi, M. 2023, Class. Quant. Grav., 40, 203001,  
 545 doi: [10.1088/1361-6382/acf28c](https://doi.org/10.1088/1361-6382/acf28c)
- 546 Isi, M., Farr, W. M., & Varma, V. 2023, Data and software  
 547 release for “The directional isotropy of LIGO-Virgo  
 548 binaries”. <https://github.com/maxisi/gwisotropy/>
- 549 Kidder, L. E. 1995, Phys. Rev. D, 52, 821,  
 550 doi: [10.1103/PhysRevD.52.821](https://doi.org/10.1103/PhysRevD.52.821)
- 551 Loredo, T. J. 2004, AIP Conf. Proc., 735, 195,  
 552 doi: [10.1063/1.1835214](https://doi.org/10.1063/1.1835214)
- 553 Luger, R., Bedell, M., Foreman-Mackey, D., et al. 2021,  
 554 arXiv e-prints, arXiv:2110.06271.  
<https://arxiv.org/abs/2110.06271>
- 555 Madau, P., & Dickinson, M. 2014, Ann. Rev. Astron.  
 556 Astrophys., 52, 415,  
 558 doi: [10.1146/annurev-astro-081811-125615](https://doi.org/10.1146/annurev-astro-081811-125615)
- 559 Mandel, I., Farr, W. M., & Gair, J. R. 2019, Mon. Not.  
 560 Roy. Astron. Soc., 486, 1086, doi: [10.1093/mnras/stz896](https://doi.org/10.1093/mnras/stz896)
- 561 Martin, O. A., Hartikainen, A., Abril-Pla, O., et al. 2023,  
 562 ArviZ, v0.15.1, Zenodo, doi: [10.5281/zenodo.7703176](https://doi.org/10.5281/zenodo.7703176)
- 563 Miller, S., Callister, T. A., & Farr, W. 2020, Astrophys. J.,  
 564 895, 128, doi: [10.3847/1538-4357/ab80c0](https://doi.org/10.3847/1538-4357/ab80c0)
- 565 Okounkova, M., Isi, M., Chatzioannou, K., & Farr, W. M.  
 566 2023, Phys. Rev. D, 107, 024046,  
 567 doi: [10.1103/PhysRevD.107.024046](https://doi.org/10.1103/PhysRevD.107.024046)
- 568 Payne, E., Banagiri, S., Lasky, P., & Thrane, E. 2020, Phys.  
 569 Rev. D, 102, 102004, doi: [10.1103/PhysRevD.102.102004](https://doi.org/10.1103/PhysRevD.102.102004)
- 570 Poisson, E., & Will, C. M. 2014, Gravity: Newtonian,  
 571 post-newtonian, relativistic (Cambridge University Press)
- 572 Pratten, G., Husa, S., Garcia-Quiros, C., et al. 2020, Phys.  
 573 Rev. D, 102, 064001, doi: [10.1103/PhysRevD.102.064001](https://doi.org/10.1103/PhysRevD.102.064001)
- 574 Pratten, G., et al. 2021, Phys. Rev. D, 103, 104056,  
 575 doi: [10.1103/PhysRevD.103.104056](https://doi.org/10.1103/PhysRevD.103.104056)
- 576 Punturo, M., et al. 2010, Class. Quant. Grav., 27, 194002,  
 577 doi: [10.1088/0264-9381/27/19/194002](https://doi.org/10.1088/0264-9381/27/19/194002)
- 578 Reitze, D., et al. 2019, Bull. Am. Astron. Soc., 51, 035.  
<https://arxiv.org/abs/1907.04833>
- 580 Romero-Shaw, I. M., et al. 2020, Mon. Not. Roy. Astron.  
 581 Soc., 499, 3295, doi: [10.1093/mnras/staa2850](https://doi.org/10.1093/mnras/staa2850)
- 582 Singer, L. 2018, ligo.skymap.  
<https://pypi.org/project/ligo.skymap/>
- 583 Singer, L. P., et al. 2016a, Astrophys. J. Lett., 829, L15,  
 585 doi: [10.3847/2041-8205/829/1/L15](https://doi.org/10.3847/2041-8205/829/1/L15)
- 586 —. 2016b, Astrophys. J. Suppl., 226, 10,  
 587 doi: [10.3847/0067-0049/226/1/10](https://doi.org/10.3847/0067-0049/226/1/10)
- 588 Stiskalek, R., Veitch, J., & Messenger, C. 2021, Mon. Not.  
 589 Roy. Astron. Soc., 501, 970, doi: [10.1093/mnras/staa3613](https://doi.org/10.1093/mnras/staa3613)
- 590 Virtanen, P., et al. 2020, Nature Meth., 17, 261,  
 591 doi: [10.1038/s41592-019-0686-2](https://doi.org/10.1038/s41592-019-0686-2)
- 592 Vitale, S., Biscoveanu, S., & Talbot, C. 2022.  
<https://arxiv.org/abs/2204.00968>

594 Wiecki, T., Salvatier, J., Vieira, R., et al. 2023,  
595    pymc-devs/pymc: v5.3.1, v5.3.1, Zenodo,  
596    doi: [10.5281/zenodo.7868623](https://doi.org/10.5281/zenodo.7868623)

597

## APPENDIX

598     A. COMPUTING THE TOTAL ANGULAR  
599         MOMENTUM

600     Here we describe how to compute the total angular  
601         momentum vector  $\vec{J}$  in the celestial coordinate frame of  
602         the main text, starting from BBH parameters measured  
603         in LIGO-Virgo analyses. The total angular momentum  
604         is defined, as in Eq. (2), to be the vector sum of the  
605         orbital angular momentum  $\vec{L}$  and the dimensionful BH  
606         spins  $\vec{S}_{1/2}$ . We can thus compute  $\vec{J}$  by summing the  
607         components of  $\vec{L}$  and  $\vec{S}_{1/2}$  in some common frame with  
608         known orientation relative to our target.

609     The Cartesian components of the BH dimensionless  
610         spins,  $\vec{\chi}_{1/2} \equiv \vec{S}_{1/2}/m_{1/2}^2$  in units where  $G = c = 1$ , can  
611         be readily obtained from the LIGO-Virgo samples, in  
612         a frame in which the  $z$ -axis points along (the Newto-  
613         nian)  $\vec{L}$  and the  $x$ -axis points along the orbital vector  
614         from the lighter to the heavier body (Creighton et al.  
615         2008) (see, e.g., Fig. 18 in Isi 2023, ); this specifica-  
616         tion is established in reference to some specific point in  
617         the evolution of the system, e.g., when the GW signal  
618         at the detector reaches some frequency  $f_{\text{ref}}$ . With that  
619         information, all we need to compute the components of  
620          $\vec{J}$  in that same frame is the magnitude  $|L|$  of the orbital  
621         angular momentum; then, the  $\vec{J}$  vector will be specified  
622         by

$$623 \quad J_x = S_{1,x} + S_{2,x}, \quad (\text{A1a})$$

$$624 \quad J_y = S_{1,y} + S_{2,y}, \quad (\text{A1b})$$

$$625 \quad J_z = S_{1,z} + S_{2,z} + |L|, \quad (\text{A1c})$$

627     and  $\vec{J} = J_x \hat{x} + J_y \hat{y} + J_z \hat{L}$ , where  $\hat{L} \equiv \vec{L}/|L|$  is the direc-  
628         tion of the orbital angular momentum,  $\hat{x}$  is the orbital  
629         vector at the reference time, and  $\hat{y}$  completes the triad.

630     In the above equations,  $(S_{1/2,x}, S_{1/2,y}, S_{1/2,z})$  are the  
631         components of the dimensionful spins, which we can de-  
632         rive from the respective components of the dimension-  
633         less spins  $\vec{\chi}_{1/2}$  using the masses  $m_{1/2}$  and the definition  
634         above. Following the standard LIGO-Virgo calculation  
635         (Creighton et al. 2008),<sup>6</sup> we can approximate the magni-  
636         tude of the orbital angular momentum as (Kidder 1995;  
637         Bohe et al. 2013)

$$638 \quad |L| = L_N (1 + \ell_{1\text{PN}}), \quad (\text{A2})$$

<sup>6</sup> Here we are following the definition of  $|L|$  within the LIGO-Virgo software; this is adopted in defining the inclination parameters  $\theta_{JN}$  and  $\iota$ . The effect of truncating the series at the first post-Newtonian order is expected to be small, but could be revisited in future work.

639     where  $L_N = m_1 m_2 / v$  is the Newtonian angular mo-  
640         mentum,  $v = (\pi M f_{\text{ref}})^{1/3}$  is the post-Newtonian expan-  
641         sion parameter at the reference frequency, and  $\ell_{1\text{PN}} =$   
642          $v^2 (3 + \eta/3)/2$  is the first-order correction to  $|L|$ , for the  
643         symmetric mass ratio  $\eta \equiv m_1 m_2 / M^2$  and the total mass  
644          $M \equiv m_1 + m_2$ . We can then get the components of the  
645         orientation vector  $\hat{J} \equiv \vec{J}/|J|$  by normalizing Eq. (A1).

646     The components of  $\vec{J}$  in Eq. (A1) are defined in a  
647         binary-specific frame which does not facilitate compar-  
648         isons across different systems. To express  $\vec{J}$  in a com-  
649         mon frame for all binaries, all we need is to express the  
650          $(\hat{x}, \hat{y}, \hat{L})$  coordinate basis of Eq. (A1) in a Celestial co-  
651         ordinate frame. We can achieve this by first obtaining  
652         the Cartesian components for  $\vec{L}$  in this frame using the  
653         measured right ascension  $\alpha$ , declination  $\delta$ , inclination  $\iota$ ,  
654         polarization angle  $\psi$ , and the reference orbital phase  $\phi_{\text{ref}}$   
655         (see, e.g., Figs. 6 and 8 Isi 2023). In doing so, however, it  
656         is important to keep in mind that, since the polarization  
657         angle only enters the waveform as  $2\psi$  (i.e.,  $\psi$  and  $\psi + \pi$   
658         are degenerate), the LIGO-Virgo analyses usually only  
659         allow  $0 \leq \psi < \pi$ ; yet,  $\psi$  and  $\psi + \pi$  are two physically dis-  
660         tinct configurations, so we must for our purposes mirror  
661         the samples to ensure they span the full range of polar-  
662         ization angles,  $0 \leq \psi < 2\pi$  (or, equivalently, randomly  
663         add  $0$  or  $\pi$  to  $\psi$  for each sample).

664     Having properly accounted for this degeneracy,  $\hat{L}$  can  
665         be obtained from the source location  $\hat{N} \equiv -\hat{k}$  in Eq. (1),  
666          $\iota$  and  $\psi$  via rotations and geometric products as

$$667 \quad \hat{L} = R_{\hat{w}_y}(\iota) \hat{k}, \quad (\text{A3})$$

668     where  $R_{\hat{v}}(\theta)$  is a right-handed rotation by an angle  
669          $\theta$  around some direction  $\hat{v}$ , and  $\hat{w}_y \propto \hat{k} \times \hat{w}_x$  with  
670          $\hat{w}_x = R_{\hat{k}}(\psi) \hat{u}$ , for  $\hat{u}$  due west (see (Anderson et al. 2002)  
671         for details). We can similarly obtain  $\hat{x}$  by rotating  $\hat{w}_y$   
672         around  $\hat{L}$  by  $\phi_{\text{ref}}$ , namely

$$673 \quad \hat{x} = R_{\hat{L}}(\phi_{\text{ref}}) \hat{w}_y, \quad (\text{A4})$$

674     and  $\hat{y} \propto \hat{L} \times \hat{x}$  completes the triad. This provides ex-  
675         pressions for the components of the  $(\hat{x}, \hat{y}, \hat{L})$  basis for  
676         each binary in a common reference frame, from which  
677         we can obtain the components of all  $\hat{J}$  vectors in that  
678         same frame via Eq. (A1). Those components are the  
679         input for the hierarchical analysis described in the main  
680         text.

681     B. PRIOR IN UNCONSTRAINED PARAMETERS

682     Recall that we sample in parameters  $\vec{u}_{N/J}$  defined by

$$683 \quad \vec{u}_{N/J} = \frac{\vec{v}_{N/J}}{\sqrt{1 - \vec{v}_{N/J} \cdot \vec{v}_{N/J}}} \quad (\text{B5})$$

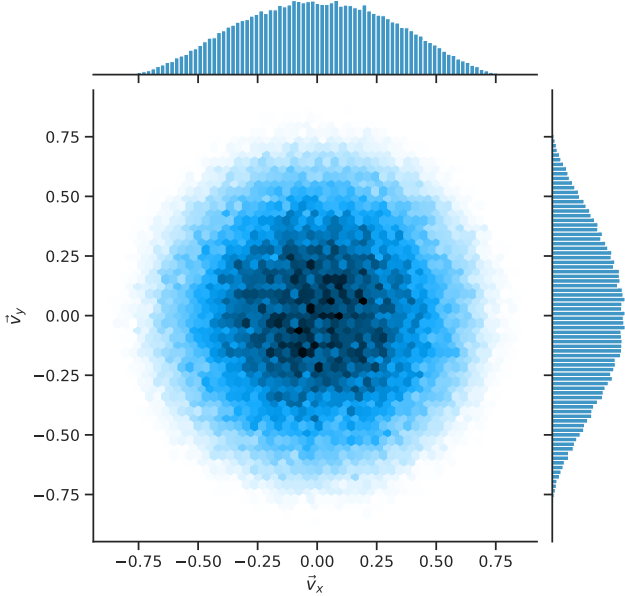


**Figure 7.** *Prior.* Two-dimensional slice of the Gaussian prior on the components of  $\vec{v}_{J/N}$  for  $\sigma = 0.4$ , as used for the analysis in the main paper. With this choice, the origin is not disfavored by the three-dimensional prior probability density.

that map the unit ball  $\mathbb{B}^3$  to  $\mathbb{R}^3$ . A Gaussian prior with mean  $\vec{0}$  and standard deviation in each component of  $\sigma$  on  $\vec{u}_{N/J}$  induces a prior on  $\vec{v}_{N/J}$  that is

$$\log p(\vec{v}_{N/J}) = \text{const} - \frac{|\vec{v}_{N/J}|^2}{2\sigma^2(1 - |\vec{v}_{N/J}|^2)} - \frac{5}{2} \log(1 - |\vec{v}_{N/J}|^2). \quad (\text{B6})$$

The derivative of the density with respect to  $|\vec{v}_{N/J}|$  vanishes at the origin, as it must by symmetry. But the second derivative does not, and is

$$\frac{\partial^2 \log p}{\partial |\vec{v}_{N/J}|^2} = 5 - \frac{1}{\sigma^2}. \quad (\text{B7})$$

Thus, such a Gaussian prior will have a *maximum* at  $\vec{v}_{N/J} = \vec{0}$  only if  $\sigma < 1/\sqrt{5} \simeq 0.45$ ; otherwise it places too much prior mass on large  $|\vec{u}_{N/J}|$  which generates a ring-shaped maximum in the prior for some  $|\vec{v}_{N/J}| > 0$  and a *minimum* at the origin. With the desire to be uninformative about the typical scale of the components of  $\vec{v}_{N/J}$  while keeping the maximum prior density at the origin, we choose  $\sigma = 0.4 < 1/\sqrt{5}$  for the analysis in this paper. A two-dimensional slice of the prior on the components of  $\vec{v}_{N/J}$  for this choice is illustrated in Fig. 7.

### C. DIRECTION OF TOTAL ANGULAR MOMENTUM FOR INDIVIDUAL EVENTS

In Fig. 8, we present posteriors on the direction of the total angular momentum  $\hat{J}$  for all 57 events in our set. We produced these posteriors by applying the calculation described in Appendix A to the samples released by LIGO-Virgo (Abbott et al. 2022, 2021e), after reweighting as outlined in Sec. 2.2.

The skymaps in the figure provide a Molleweide projection of probability density over the celestial sphere, in the standard equatorial, geocentric coordinates used in the main text. A darker color corresponds to a direction in the sky with more probability density. From these maps, it is clear that not all events are equally informative about  $\hat{J}$ ; better constrained events will tend to dominate our hierarchical measurement.

The skymaps were produced using the LIGO.SKYMAPP package (Singer 2018; Singer et al. 2016a,b), a set of standard LIGO-Virgo tools for the processing of probability densities over the sphere. We make these figures, corresponding Flexible Image Transport System (FITS) files, and code used to generate them, available in our data release (Isi et al. 2023).

### D. REPRODUCIBILITY

This study was carried out using the reproducibility software **show your work!** (Luger et al. 2021), which leverages continuous integration to programmatically download the data from zenodo.org, create the figures, and compile the manuscript. Each figure caption contains two types of links: one to the dataset stored on Zenodo used in the corresponding figure, and the other to the script used to make the figure (at the commit corresponding to the current build of the manuscript). The git repository associated with this study is publicly available at <https://github.com/maxisi/gwisotropy> and the Zenodo archive <https://doi.org/10.5281/zenodo.10146082>. The datasets are stored at <https://doi.org/10.5281/zenodo.7775266>.

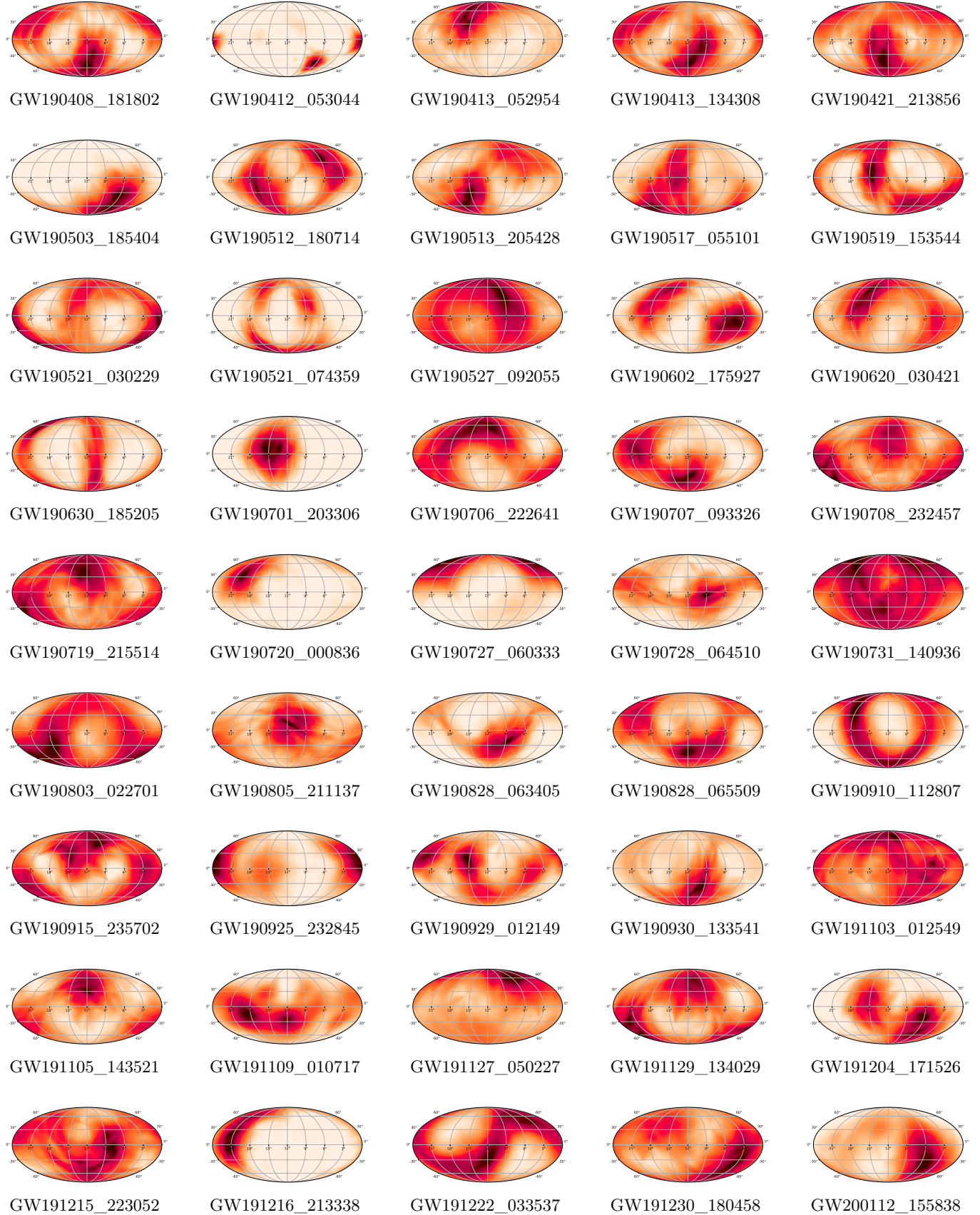


**Figure 8.** Measurements of the total angular momentum direction,  $\hat{J}$ , for the events in our set, in a Mollweide projection of Earth-centric Celestial coordinates; darker color represents higher probability density for that direction in space.

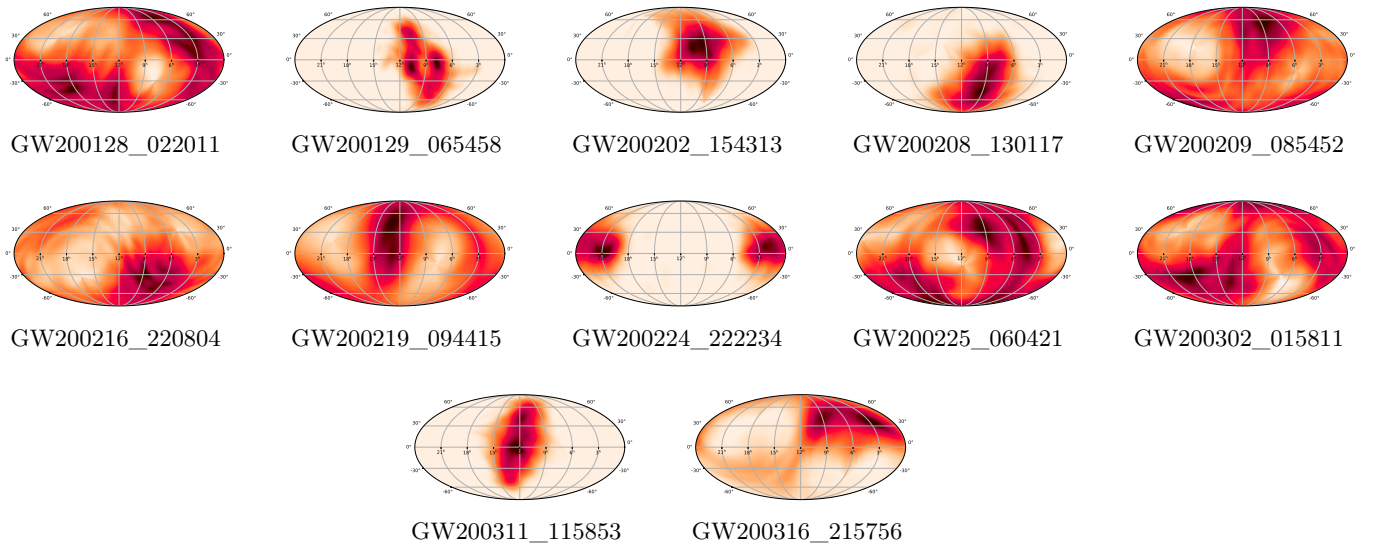


**Figure 8.** Measurements of the total angular momentum direction,  $\hat{J}$ , for the events in our set, in a Mollweide projection of Earth-centric Celestial coordinates; darker color represents higher probability density for that direction in space (cont.).